Available online at www.sciencedirect.com
ScienceDirect
Journal of Sound and Vibration 319 (2009) 491–514
JOURNAL OF SOUND AND VIBRATION
www.elsevier.com/locate/jsvi

Torsional vibration of crankshaft in an engine–propeller nonlinear dynamical system

X. Zhang, S.D. Yu*

Department of Mechanical and Industrial Engineering, Ryerson University, 350 Victoria Street, Toronto, Ont., Canada M5B 2K3

Received 19 February 2007; received in revised form 30 April 2008; accepted 3 June 2008
Handling Editor: S. Bolton
Available online 7 July 2008

Abstract

Theoretical and experimental studies on torsional vibration of an aircraft engine–propeller system are presented in this paper. Two system models—a rigid body model and a flexible body model, are developed for predicting torsional vibrations of the crankshaft under different engine powers and propeller pitch settings. In the flexible body model, the distributed torsional flexibility and mass moment of inertia of the crankshaft are considered using the finite element method. The nonlinear autonomous equations of motion for the engine–propeller dynamical system are established using the augmented Lagrange equations, and solved using the Runge–Kutta method after a degrees of freedom reduction scheme is applied. Experiments are carried out on a three-cylinder four-stroke engine. Both theoretical and experimental studies reveal that the crankshaft flexibility has significant influence on the system dynamical behavior.

1. Introduction

Significant torsional vibration and dynamic shear stresses often occur in the crankshaft of an engine–propeller drive system. The crankshaft torsional vibration is the leading cause for its failure. The engine manufacturers are required by transportation authorities to certify the magnitudes of torsional vibrations and shear stresses in the crankshaft through tests for each application. To reduce the costs associated with the expensive and exhaustive tests designed to cover various normal and abnormal operating conditions, it is often desirable to have a computer code for theoretical predictions of stresses in the crankshaft. Once validated, the computer simulation results can be used in conjunction with a selected set of test results for the certification purpose.

In some early work on torsional vibrations [1–4], crankshaft models were developed in an isolated manner. The engine was treated as a rigid block. The gas torque and the loads were considered as the prescribed functions of time. Natural frequencies and responses of the crankshaft were calculated using the Holzer method, the transfer matrix method or the finite element method. The dynamic coupling among different components is often ignored in these models so that the system equations of motion can be simplified as linear

*Corresponding author. Tel.: +1 416 979 5000x7687; fax: +1 416 979 5265.
E-mail address: syu@ryerson.ca (S.D. Yu).

0022-460X/$ - see front matter © 2008 Elsevier Ltd. All rights reserved.
doi:10.1016/j.jsv.2008.06.004

Nomenclature

A_p	piston top area (m^2)
$\mathbf{C}$	global constraint matrix
$\mathbf{C}_n$	constraint matrix at interface n
D_e	geometric matrix
$\mathbf{g}$	constraint vector
$\mathbf{G}$	derivative matrix of the constraint vector
G	shear modulus (Pa)
$\mathbf{h}$	nonlinear terms in the system equations of motion
I	mass moment of inertia of the engine block ($kg\,m^2$)
I'	derivative of I with respect to the crankshaft angular position at the engine–propeller interface ($kg\,m^2\,rad^{-1}$)
I_c	mass moment of inertia of the counterweight and the crank pin ($kg\,m^2$)
$I_{G,i}$	mass moment of inertia of the ith connecting rod ($i = 1, 2, 3$) ($kg\,m^2$)
I_p	mass moment of inertia of the propeller assembly ($kg\,m^2$)
$\overline{I}_0$	Fourier coefficient of the constant term for the effective mass moment of inertia of the engine block
$\overline{I}_k$	Fourier coefficient of the kth cosine term for the effective mass moment of inertia of the engine block ($k = 1,\ldots,40$)
$\hat{I}_k$	Fourier coefficient of the kth sine term for the effective mass moment of inertia of the engine block ($k = 1,\ldots,40$)
J	polar moment of cross sectional area (m^4)
K	system stiffness matrix
$\mathbf{K}_c$	crankshaft stiffness matrix
$\mathbf{K}_e$	element stiffness matrix
$\mathbf{K}_s$	segment stiffness matrix
l_e	element length (m)
L	Lagrangian
$m_{P,i}$	mass of the ith piston ($i = 1, 2, 3$) (kg)
$m_{R,i}$	mass of the ith connecting rod ($i = 1, 2, 3$)
$\mathbf{M}$	system mass matrix
$\mathbf{M}_c$	crankshaft mass matrix
$\mathbf{M}_e$	element mass matrix
$\mathbf{M}_s$	segment mass matrix
$\mathbf{N}$	shape function
p_i	pressure in the ith cylinder ($i = 1, 2, 3$) (Pa)
$\mathbf{q}$	generalized force
Q	gas torque (N m)
Q_p	aerodynamic torque of the propeller (N m)
$\overline{Q}_0$	Fourier coefficient of the constant term for the gas torque
$\overline{Q}_k$	Fourier coefficient of the kth cosine term for the gas torque ($k = 1, \ldots, 40$)
$\hat{Q}_k$	Fourier coefficient of the kth sine term for the gas torque ($k = 1, \ldots, 40$)
$r_{G,j}$	position of the mass center of the jth connecting rod in the engine block ($j = 1, 2, 3$)
R	segment radius (m)
s_i	piston position ($j = 1, 2, 3$) (m)
T	kinetic energy of the system (J)
T_1	kinetic energy of the engine block (J)
T_c	kinetic energy of the crankshaft (J)
T_e	kinetic energy of an element (J)
T_p	kinetic energy of the propeller assembly (J)
$\mathbf{T}_s$	transformation matrix
$v_{P,i}$	velocity of the ith piston ($i = 1, 2, 3$) ($m\,s^{-1}$)
$v_{G,i}$	velocity of the mass center of the ith connecting rod ($i = 1, 2, 3$) ($m\,s^{-1}$)
V	potential energy of the system (J)
V_c	potential energy of the crankshaft (J)
V_e	potential energy of a finite element (J)
$\mathbf{x}$	modal coordinates
x	global axial coordinate (m)
α_1	polynomial coefficient for the propeller aerodynamic torque
α_2	polynomial coefficient for the propeller aerodynamic torque
ζ	local axial coordinate (m)
$\mathbf{\Lambda}_i$	natural frequency matrix of the internal structure
$\boldsymbol{\theta}$	generalized coordinates for the entire crankshaft
θ	angular position of the crankshaft at an axial location (rad or deg)
$\boldsymbol{\theta}^{(i)}$	independent generalized coordinates
$\boldsymbol{\theta}^{(d)}$	dependent generalized coordinates
θ_1	angular position of the interface between the engine block and the crankshaft (rad or deg)
$\boldsymbol{\theta}_e$	generalized coordinates in an element
$\boldsymbol{\theta}_t$	internal generalized coordinates
$\boldsymbol{\theta}_f$	interface generalized coordinates
$\boldsymbol{\theta}_p$	angular position of the interface between the propeller assembly and the crankshaft (rad or deg)
$\boldsymbol{\theta}_s$	generalized coordinates in a segment

ϕ_j	angular positions of three connecting rods ($j = 1, 2, 3$)	$\mathbf{\Phi}_f$	interface modal matrix
		$\boldsymbol{\lambda}$	Lagrange multiplier vector
$\mathbf{\Phi}_t$	internal modal matrix	ρ	density ($\mathrm{kg\,m^{-3}}$)

equations. The natural frequencies obtained from an individual crankshaft with pre-assumed boundary conditions may not be real due to the varying interface conditions. Recently, sophisticated nonlinear models involving the coupling of the crankshaft motion on the engine block have been developed. Pasricha and Carnegie [5] modeled the changing inertia of a multi-cylinder engine. Their model did not involve driving forces and loads. Brusa et al. [6] considered the effect of the changing inertia and prescribed time-dependent forcing functions in a crankshaft torsional vibration analysis. More advanced models can be found in Refs. [7,8], which involve the changing inertia and external forces as functions of crankshaft motion. However, the crankshaft is treated as a rotational spring in their models. In another model [9], the crankshaft deformation is described using finite elements and modal coordinates. The modal vectors obtained by ignoring the changing inertia of the engine block are used to approximate the true rotation-dependent modal vectors. Hoffman and Dowling [10] developed a model for internal combustion engine to involve all the above nonlinearities, but crankshaft flexibility is not considered in that model.

Strong nonlinear terms [11] are present in an engine–propeller dynamical system when the effect of changing inertia of the engine and the speed-dependent aerodynamic load from the propeller are considered. The system response exhibits sub- and super-harmonic components with reference to the mean angular speed of the crankshaft. Presence of the nonlinear factors along with the crankshaft complex geometries makes it hard to seek an accurate analytical solution for the torsional vibration problem.

When one or more flexible bodies in a multibody dynamical system are modeled using finite elements, this usually results in a large number of degrees of freedom and leads to unbearable computation cost [12]. This problem is especially true in dealing with nonlinear dynamic system because efficient integration algorithms, such as the Newmark method, lose accuracy. To reduce the number of degrees of freedom while retaining a high degree of accuracy, reduction techniques are often used. The component mode synthesis is commonly used in a dynamic analysis. The displacements within a substructure (component) are described by combinations of assumed basis vectors, known as the component modes [13]. System equations are transformed from the physical space to the modal space. To reduce the degrees of freedom, some modes for the component (usually the inaccurate high-frequency modes) are ignored and only the desired modes are kept. The component modes can be the eigenvectors of the component or the Ritz vectors. The component mode synthesis was first proposed by Hurty in the 1960s [14] and improved by Craig and Bampton [15]. An application of this type of reduction scheme in the crankshaft-engine analysis can be found in Ref. [16].

In this paper, a coupled rigid and kineto-elasto-dynamic model is developed for an engine–propeller system shown in Fig. 1. The engine is regarded as a system of rigid bodies. The stepped crankshaft is modeled using the three-node torsional finite elements. The aerodynamic torque is obtained using the blade element theory. The aerodynamic torque varies with the instant angular speed at the interface between the crankshaft and the propeller. A set of nonlinear equations of motion is obtained using the augmented Lagrange equations. Component mode synthesis is then applied to the equations of motion to produce a small-scale model without weakening the nonlinearities. Runge–Kutta algorithm is used to determine the transient and steady state responses of the reduced model.

A Saito-450 glow assisted methanol engine, a SOLO 24″ propeller and various control devices, are set up for experimental studies of the crankshaft motions. A 64-tooth magnetic encoder is installed on the torque plate to monitor the crankshaft transient velocity. Pulse signals generated when the magnetic teeth pass a sensing unit are collected by an A/D device with a sampling rate high enough to restore the pulse profile. Linear interpolation is used to find the arrival time for each magnetic tooth from the pulse profile, and the angular position vs. time relationship is therefore obtained. An adaptive cubic polynomial interpolation scheme is used to resample the uneven spaced angular position vs. time series, so that finite difference and fast Fourier analysis can be applied to the signal.

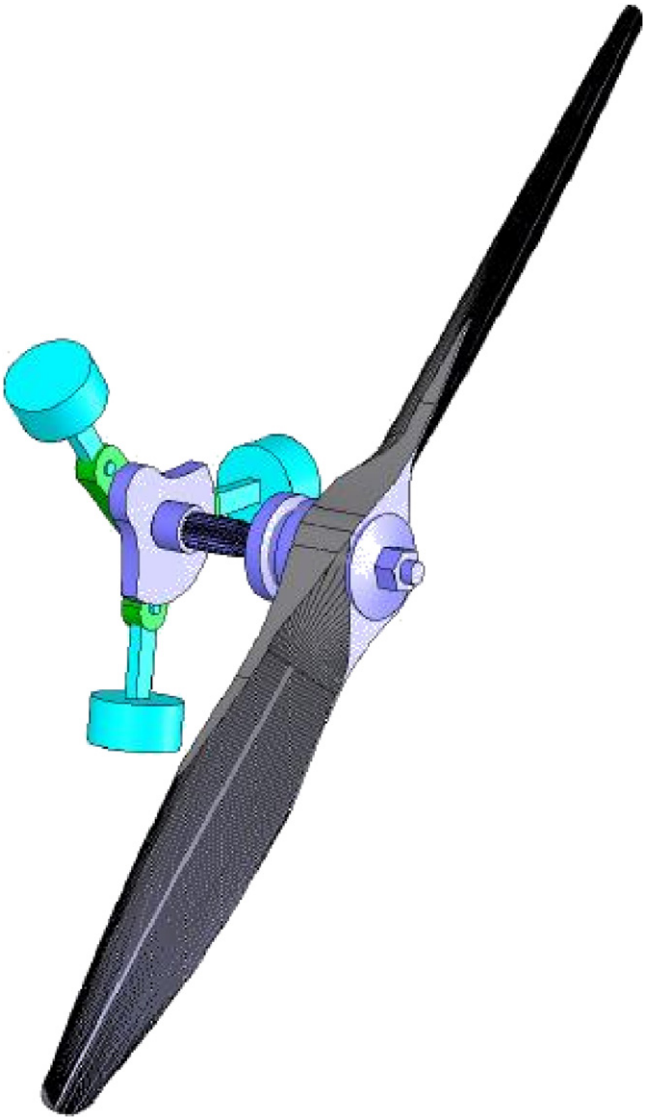

Fig. 1. Illustration of a Saito-R450 engine and SOLO propeller system.

2. System modeling

2.1. Engine kinematics

The engine studied in this paper is a 4.25 cubic inch, 7 horse power, four-stroke radial Saito-450 engine. The Saito-450 engine mechanism is a planar 8-bar linkage shown in Fig. 2. The eight bars are the ground, three pistons, the master connecting rod, and two slave connecting rods. In this mechanism, the gas force produced by the master cylinder is transmitted directly to the crankshaft through the master connecting rod. The gas forces produced from the second and third cylinders are transmitted to the crankshaft through the two slave rod pinned to the master connecting rod. To determine the kinetic energy, the potential energy and the gas torque at an arbitrary crank position, a kinematical analysis need to be conducted.

In the kinematical analysis, the crankshaft angular position, θ_1, measured counterclockwise from the centerline of the primary cylinder, is chosen as the generalized coordinate for the one degree of freedom (dof) rigid planar mechanism. Linear positions of the three pistons and mass centers of all moving links, and

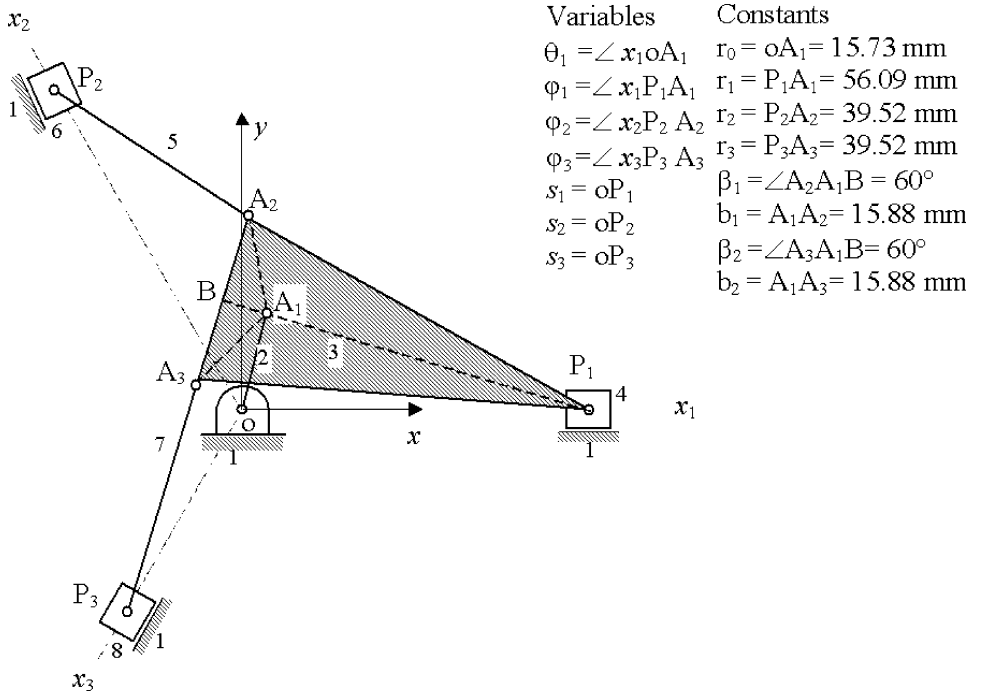

Fig. 2. The skeleton diagram of an eight-bar mechanism used in a Saito-450 engine.

angular positions of the three connecting rods are determined in terms of the crankshaft angular position. For convenience, the complex number method [17] is used to conduct displacement and velocity analyses.

For a given crankshaft angle, θ_1, the linear positions of the three pistons may be determined by the corresponding distances, $s_j, j = 1, 2, 3$, measured on their respective centerlines from the crankshaft centerline. The angular positions of the three connecting rods, $\phi_j, j = 1, 2, 3$, measured counterclockwise from the three respective centerlines may be used to determine the positions of the connecting rods. From the loop closure equations, one may relate the three linear positions and three angular positions to the generalized coordinate as follows:

$$\phi_1 = \pi - \sin^{-1}\left(\frac{r_0}{r_1}\sin\,\theta_1\right),$$
$$s_1 = r_0\cos\,\theta_1 - r_1\cos\,\phi_1, \tag{1}$$

$$\phi_2 = \pi + \sin^{-1}\left[\frac{r_0}{r_2}\sin\left(\frac{2\pi}{3} - \theta_1\right) + \frac{b_1}{r_2}\sin\left(\frac{2\pi}{3} - \phi_1 + \beta_1\right)\right],$$
$$s_2 = \cos^{-1}\frac{2\pi}{3}\left[r_0\cos\,\theta_1 + b_1\cos(\phi_1 - \beta_1) - r_2\cos\left(\frac{2\pi}{3} + \phi_2\right)\right], \tag{2}$$

$$\phi_3 = \pi + \sin^{-1}\left[\frac{r_0}{r_3}\sin\left(\frac{4\pi}{3} - \theta_1\right) + \frac{b_2}{r_3}\sin\left(\frac{4\pi}{3} - \phi_1 - \beta_2\right)\right],$$
$$s_3 = \cos^{-1}\frac{4\pi}{3}\left[r_0\cos\,\theta_1 + b_2\cos(\phi_1 + \beta_2) - r_3\cos\left(\frac{4\pi}{3} + \phi_3\right)\right], \tag{3}$$

where link lengths and angles are defined in Fig. 2.

From the above equations, the strokes of the three pistons are 31.5, 31.9, and 31.9 mm. A small difference of 0.4 mm is observed between the stroke of the master piston and the strokes of the two secondary pistons.

To avoid dealing with lengthy formulas for velocities and accelerations, it was decided to determine the velocities using a higher order central difference method. The linear velocities of the three pistons and the angular velocities of the three connecting rods are determined at an arbitrary crankshaft angular position:

$$\frac{\mathrm{d}\phi_i}{\mathrm{d}t}=\dot{\theta}_1\frac{\mathrm{d}\phi_i}{\mathrm{d}\theta_1}=\dot{\theta}_1\left\{\frac{-\phi_i|_{\theta_1+2\Delta\theta_1}+8\phi_i|_{\theta_1+\Delta\theta_1}-8\phi_i|_{\theta_1-\Delta\theta_1}+\phi_i|_{\theta_0-2\Delta\theta_1}}{12\Delta\theta_1}\right\},$$
$$\frac{\mathrm{d}s_i}{\mathrm{d}t}=\dot{\theta}_1\frac{\mathrm{d}s_j}{\mathrm{d}\theta_1}=\dot{\theta}_1\left\{\frac{-s_i|_{\theta_1+2\Delta\theta_1}+8s_i|_{\theta_1+\Delta\theta_1}-8s_i|_{\theta_1-\Delta\theta_1}+s_i|_{\theta_1-2\Delta\theta_1}}{12\Delta\theta_1}\right\}, \tag{4}$$

where $\Delta\theta_1$ is the angular step. To ensure accuracy, its value has been taken to be 0.0351° for all simulations in this paper.

Linear velocities of the mass centers of the three connecting rods may be determined from the analyses of the fundamental displacements and velocities. From the measurements taken on the individual connecting rods, the mass center (GB_j) of each of the three connecting rods for the Saito-450 engine is located on P_jG_j, $r_{G,1}=43.0\,\mathrm{mm}$, $r_{G,2}=r_{G,3}=10.9\,\mathrm{mm}$, as shown in Fig. 2. Distances $r_{G,j}$ between G_j and the crankpin P_j are sufficient to locate the mass centers of the three connecting rods. The velocities of the three mass centers may be found from the following equations:

$$v_{G,1}=\dot{s}_1+r_{G,1}\dot{\phi}_1\,\mathrm{e}^{\mathrm{i}(\phi_1+\pi/2)},\quad v_{G,2}=\dot{s}_2\,\mathrm{e}^{\mathrm{i}2\pi/3}+r_{G,2}\dot{\phi}_2\,\mathrm{e}^{\mathrm{i}(2\pi/3+\phi_2+\pi/2)},\quad v_{G,3}=\dot{s}_3\,\mathrm{e}^{\mathrm{i}4\pi/3}+r_{G,3}\dot{\phi}_3\,\mathrm{e}^{\mathrm{i}(4\pi/3+\phi_3+\pi/2)}. \tag{5}$$

By taking the sum of the kinetic energy of all the components, the kinetic energy of the engine block, T_1, can be written as

$$T_1=\sum_{i=1}^{3}\left[\frac{1}{2}m_{R,i}v_{G,i}^2+\frac{1}{2}I_{G,i}\dot{\phi}_i^2+\frac{1}{2}m_{P,i}v_{P,i}^2\right]+\frac{1}{2}I_c\dot{\theta}_1^2=\frac{1}{2}I(\theta_1)\dot{\theta}_1^2, \tag{6}$$

where $m_{R,I}$ and $I_{G,i}$ are the mass and the mass moment of inertia about the mass center of the ith ($i=1, 2, 3$) connecting rod; $v_{G,I}$ and $\dot{\phi}_i$ are the velocity of the mass center of the ith ($i=1, 2, 3$) connecting rod and the angular velocity of that rod; $m_{P,I}$ is the mass of the ith ($i=1, 2, 3$) piston; $v_{P,I}$ is the velocity of the mass center of the ith ($i=1, 2, 3$) piston; I_c is the mass moment of inertia of the counterweight and the crank pin about the axis of the crank angle θ_1 at the engine–crankshaft interface; I is defined as the effective mass moment of inertia of the engine block.

The effective mass moment of inertia I is a 2π-period function of θ_1. To avoid using the lengthy formula, the effective mass moment of inertia is expressed in terms of Fourier series as

$$I=\overline{I}_0+\sum_{k=1}^{40}(\overline{I}_k\cos k\theta_1+\hat{I}_k\sin k\theta_1), \tag{7}$$

where $\overline{I}_0$, $\overline{I}_k$ and $\hat{I}_k$, ($k=1, \ldots, 40$), are Fourier coefficients. The values of I are obtained at 1024 mechanism configurations in a cycle of 2π. The Fourier coefficients are then determined using the fast Fourier transform algorithm [18]. Because of the smooth variations of I with the crankshaft angular position, the Fourier series converge rapidly with the number of terms. It was decided to use 40 terms in the Fourier series, which is enough to achieve sufficient accuracy. The converged Fourier series for the effective mass moment of inertia and its derivative with respect to θ_1 are shown in Figs. 3 and 4, respectively. Parameters that are necessary for the above analysis are given in Table 1.

2.2. Gas torque

The driving force of the system is the gas pressure in each cylinder. The crankshaft angle at the crankshaft-engine interface of the intake, compression, expansion and exhaust processes are measured and the pressure rise due to the polytropic process in compression and expansion stroke are determined with the exhaust gas temperature measured at the exhaust outlet. The additional pressure rise due to combustion is approximated by a polynomial with assumed combustion starting and completing crankshaft angles. Since two glow plugs

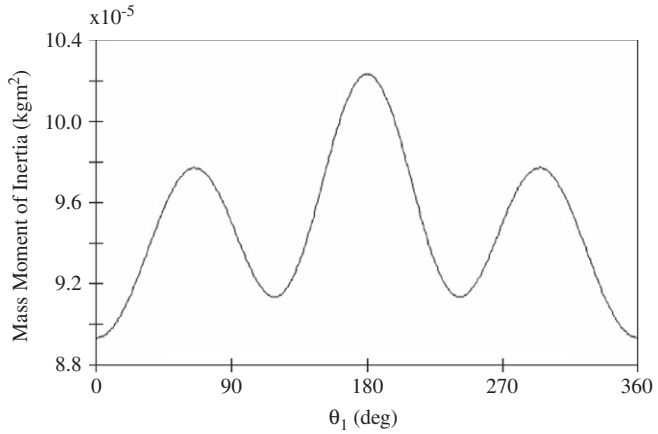

Fig. 3. Variation of engine effective mass moment of inertia throughout a cycle.

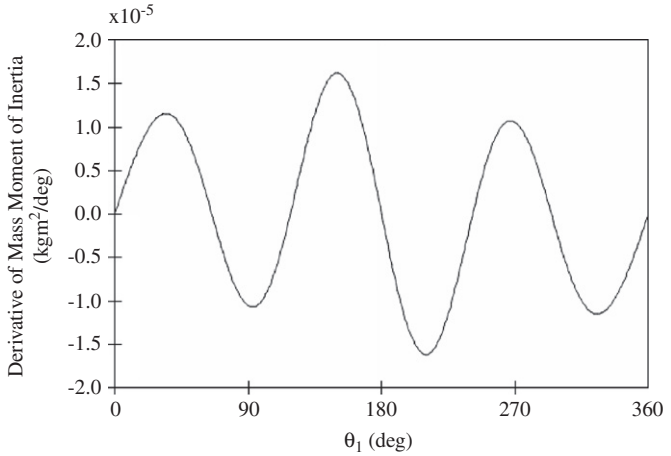

Fig. 4. Variation of derivative of engine effective mass moment of inertia throughout a cycle.

Table 1
Mass and mass moment of inertia of the components in the engine

Part	Component # in Fig. 2	Mass (kg)	Moment of inertia about mass center ($kg\,m^2$)	Position of mass center (mm)
Piston #1 + wrist pin	4	0.02436	–	–
Piston #2 + wrist pin	6	0.02436	–	–
Piston #3 + wrist pin	8	0.02436	–	–
Counterweight	–	0.12095	5.8679×10^{-5a}	–
Crank pin	–	0.00981	2.7122×10^{-6b}	–
Master connecting rod	3	0.03109	1.5347×10^{-5b}	14.0 from A_1
Secondary connecting rod + pin (piston #2)	5	0.001639	7.5120×10^{-6b}	16.8 from P_2
Secondary connecting rod + pin (piston #3)	7	0.001639	7.5124×10^{-6b}	16.8 from P_3

[a]Measured about the axis of rotation of the crankshaft.
[b]Measured about the mass center.

per cylinder are used to ignite the compressed gas-air mixture, it is difficult to determine precisely the start and end of the power stroke in terms of the crankshaft angle. An estimate was made in a previous paper [19] based on recommendations from Ma et al. [20] and Zweiri et al. [21]. The starting angle of the initial combustion and finishing angle of the main combustion are determined to be 35° before the top dead center (BTDC) and 40° after the top dead center (ATDC), respectively. A clamped fourth-order polynomial is used to join the two points. The peak value of the polynomial is controlled by the gas-oil mixture ratio which represents throttle opening. The gas torque can be calculated with the pressure and the kinematic relationship between the pistons position and the crankshaft angle, as

$$Q = \sum_{i=1}^{3} p_i(\theta_1) A_p \left(\frac{\partial s_i}{\partial \theta_1} \right) \tag{8}$$

where p_i is the pressure in the ith cylinder ($i = 1, 2, 3$); A_p is the piston top area (three pistons are identical); and s_i ($i = 1, 2, 3$) is the piston position. For a four-stroke engine, each cylinder fires once in two crankshaft revolutions. For a prescribed throttle setting, the generalized force associated with θ_1 (or the gas torque) is a 4π-period function of θ_1. To express the gas torque conveniently, the Fourier series is again used. Unlike the smooth-varying inertia, the gas torque varies sharply with θ_1 during the power stroke. As a result, 40 terms are used in the Fourier series representation for the gas torque under a throttle setting. It is written as

$$Q = \overline{Q}_0 + \sum_{k=1}^{40} \left(\overline{Q}_k \cos \frac{k\theta_1}{2} + \hat{Q}_k \sin \frac{k\theta_1}{2} \right) \tag{9}$$

where $\overline{Q}_0$, $\overline{Q}_k$, and $\hat{Q}_k$ ($k = 1, \ldots, 40$), are Fourier coefficients. An example of the converged gas torque in one thermodynamic cycle is shown in Fig. 5.

2.3. Aerodynamic load

The modified blade element theory is used to model the propeller aerodynamics and to take into consideration the downwash induced by the blade sections. To achieve high accuracy, the entire propeller blade is divided into 20 sections. Each section is treated as a 2-D airfoil for determining the local lift and drag forces. Contributions of individual blade stations to the overall aerodynamic torque are summed over all 20 sections for different pitch settings and operating speeds. To conduct the blade element analysis for an adjustable pitch propeller, the airfoil cross section at each station is approximated using a National Advisory Committee for Aeronautics (NACA) 4-digit airfoil. The geometric and aerodynamic twist can be obtained as a function of the blade pitch setting. All of these quantities are passed in a batch mode to the X-Foil code, which was developed by researchers at the Massachusetts Institute of Technology and made accessible via the Internet. The raw data were then best fit with a second-order polynomial in terms of propeller rotational

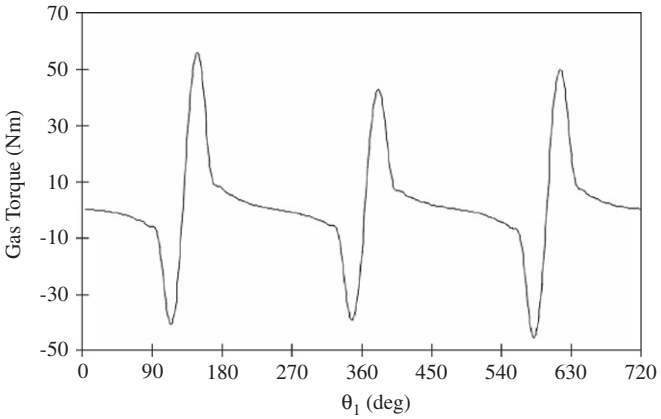

Fig. 5. Gas torque of 4π period.

speed. The propeller torque is written as

$$Q_p = \alpha_1 \dot{\theta}_p + \alpha_2 \dot{\theta}_p^2, \tag{10}$$

where $\dot{\theta}_p$ is the angular velocity of the propeller; α_1 and α_2 are constants for a pitch setting. The aerodynamic torque vs. the propeller speed is shown in Fig. 6 for three pitch settings: 4″, 6″ and 8″. This part of work was done by one of the author of this paper cooperated with Warwick in Ref. [22].

2.4. Finite element modeling of crankshaft

The crankshaft plays a pivotal role in transmitting power/torque from the engine to the propeller. To house the bearings, intake/exhaust cams, and torque plates, the crankshaft is designed to have four different segments as shown in Fig. 1. To define positions of all components in the system, a right-handed inertial coordinate system, o-*xyz* with an origin at the engine–crankshaft interface, is used. The *x*- and *y*-axes are shown in Fig. 2. The *z*-axis coincides with the crankshaft centerline, pointing out of the surface of the paper. Parameters of the crankshaft and the propeller are given in Table 2.

Three-node torsional finite elements shown in Fig. 7 are employed to model the crankshaft torsion. Each node has two degrees of freedom, namely, the angular position, θ, and its derivative with respect to z, denoted as θ'. Within a finite element, θ and θ' may be written in terms of the local coordinate ζ and the nodal variables as

$$\theta = \mathbf{N}(\zeta)\mathbf{D}_e\boldsymbol{\theta}_e, \quad \theta' = \frac{\partial \mathbf{N}(\zeta)}{\partial \zeta}\mathbf{D}_e\boldsymbol{\theta}_e, \quad 0 \leqslant \zeta \leqslant l_e, \tag{11}$$

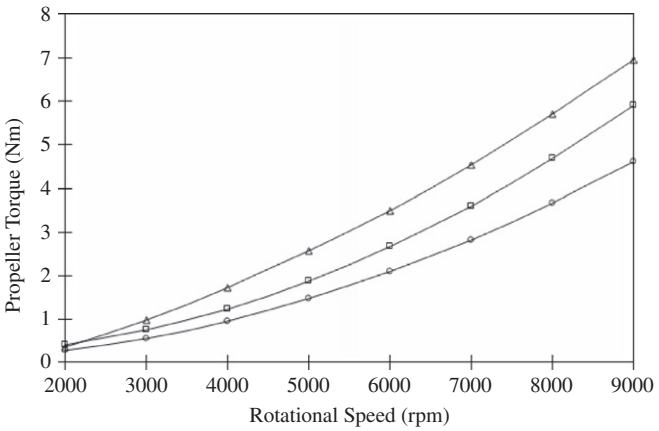

Fig. 6. Overall torque of the SOLO propeller with 4″(-○-), 6″(-□-) and 8″(-△-) pitch settings.

Table 2
Parameters of the crankshaft and the propeller

Part	Length (mm)	Radius (mm)	Mass moment of inertia (kg m^2)
Crankshaft step 1	13.0	10.0	1.59×10^{-6}
Crankshaft step 2	26.0	7.5/6.0[a]	0.76×10^{-6}
Crankshaft step 3	8.5	6.5/6.0[a]	0.18×10^{-6}
Crankshaft step 4	14.0	6.0	0.22×10^{-6}
Propeller assembly	–	–	3.40×10^{-3}

[a]Major/root radii of the spline.

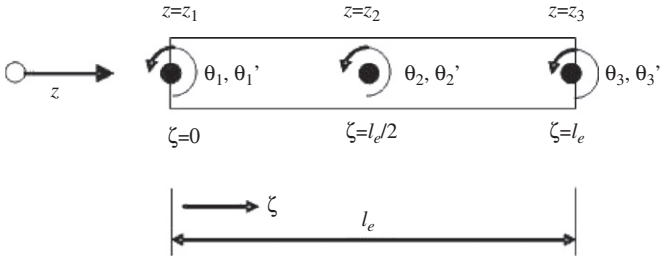

Fig. 7. A 3-node torsional finite element.

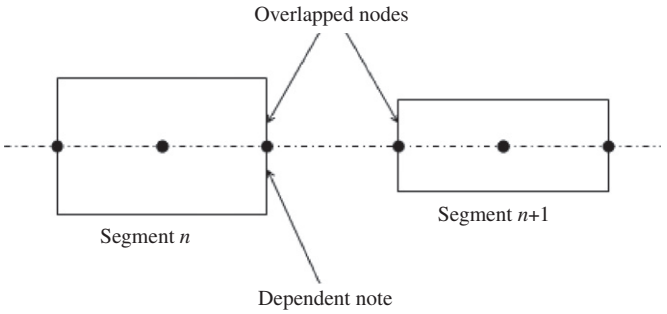

Fig. 8. Two adjacent segments.

where $\mathbf{N}(\zeta)=[1\ \ \zeta\ \ \zeta^2\ \ \zeta^3\ \ \zeta^4\ \ \zeta^5]$ is the shape function matrix; $\boldsymbol{\theta}_e=[\theta_1\ \ \theta_1'\ \ \theta_2\ \ \theta_2'\ \ \theta_3\ \ \theta_3']^{\mathrm{T}}$ is the element nodal variable vector; $\mathbf{D}_e$ is the geometric matrix, whose elements are defined as

$$\mathbf{D}_e=\begin{bmatrix} 1 & 0 & 0 & 0 & 0 & 0 \\ 0 & 1 & 0 & 0 & 0 & 0 \\ -23/l_e^2 & -6/l_e & 16l_e^2 & -8l_e & 7/l_e^2 & -1/l_e \\ 66/l_e^3 & 13/l_e^2 & -32/l_e^3 & 32/l_e^2 & -34/l_e^3 & 5/l_e^2 \\ -68/l_e^4 & -12/l_e^3 & 16/l_e^4 & -40/l_e^3 & 52/l_e^4 & -8/l_e^3 \\ 24/l_e^5 & 4/l_e^4 & 0 & 16/l_e^4 & -24/l_e^5 & 4/l_e^4 \end{bmatrix}.$$

The element kinetic energy and potential energy can be written as

$$T_e=\frac{1}{2}\int_0^{l_e}\rho J\dot{\theta}^2\,\mathrm{d}\zeta=\frac{1}{2}\dot{\boldsymbol{\theta}}_e^{\mathrm{T}}\mathbf{M}_e\dot{\boldsymbol{\theta}}_e, \tag{12}$$

$$V_e=\frac{1}{2}\int_0^{l_e}GJ\left(\frac{\partial\boldsymbol{\theta}_e}{\partial\zeta}\right)^2\mathrm{d}\zeta=\frac{1}{2}\boldsymbol{\theta}_e^{\mathrm{T}}\mathbf{K}_e\boldsymbol{\theta}_e, \tag{13}$$

where ρ is the density, G is the shear modulus, J is the polar moment of the cross sectional area, and

$$\mathbf{M}_e=\mathbf{D}_e^{\mathrm{T}}\left[\int_0^{l_e}\rho J\mathbf{N}^{\mathrm{T}}\mathbf{N}\,\mathrm{d}\zeta\right]\mathbf{D}_e,\quad \mathbf{K}_e=\mathbf{D}_e^{\mathrm{T}}\left[\int_0^{l_e}GJ\frac{\partial\mathbf{N}^{\mathrm{T}}}{\partial\zeta}\frac{\partial\mathbf{N}}{\partial\zeta}\,\mathrm{d}\zeta\right]\mathbf{D}_e.$$

The crankshaft has four segments with different radii. Since the size of the steps between adjacent segments is not small enough to be neglected. Additional constraint conditions have to be considered across the steps. To apply the constraint conditions, an interface between two adjacent segments is introduced, as shown in Fig. 8. There are two overlapped nodes on each interface. The nodal variables on these nodes are related with each other through the constraint conditions; therefore, only one of the nodes should be considered dependent to the other. For convenience, denote the nodal variables at the dependent node with superscript (d), and the variables of all

the other nodes with superscript (i). The angular displacement vector of the crankshaft can then be written as

$$\boldsymbol{\theta} = \left\{ \theta_1^{(i)} \quad \theta'^{(i)}_1 \quad \cdots \quad \theta_n^{(d)} \quad \theta'^{(d)}_n \quad \theta_n^{(i)} \quad \theta'^{(i)}_n \quad \cdots \quad \theta_p^{(i)} \quad \theta'^{(i)}_p \right\}, \tag{14}$$

where the subscript 1, n and p denotes the first node, the overlapped nodes at segment interface n, and the node at the propeller, respectively. The kinetic and potential energy of segment s can be written as

$$T_s = \frac{1}{2}\dot{\boldsymbol{\theta}}_s^{\mathrm{T}}\mathbf{M}_s\dot{\boldsymbol{\theta}}_s, \tag{15}$$

$$V_s = \frac{1}{2}\boldsymbol{\theta}_s^{\mathrm{T}}\mathbf{K}_s\boldsymbol{\theta}_s, \tag{16}$$

where $\boldsymbol{\theta}_s$ is the nodal displacement vector of segment s ($s = 1, 2, 3, 4$); $\mathbf{M}_s$ is the mass matrix of segment s; and $\mathbf{K}_s$ is the stiffness matrix of segment s.

The total kinetic and potential energies for the entire crankshaft can be written as

$$T_c = \frac{1}{2}\sum_{s=1}^{4}\dot{\boldsymbol{\theta}}_s^{\mathrm{T}}\mathbf{M}_s\dot{\boldsymbol{\theta}}_s = \frac{1}{2}\dot{\boldsymbol{\theta}}^{\mathrm{T}}\mathbf{M}_c\dot{\boldsymbol{\theta}}, \tag{17}$$

$$V_c = \frac{1}{2}\sum_{s=1}^{4}\boldsymbol{\theta}_s^{\mathrm{T}}\mathbf{K}_s\boldsymbol{\theta}_s = \frac{1}{2}\boldsymbol{\theta}^{\mathrm{T}}\mathbf{K}_c\theta, \tag{18}$$

where $\mathbf{M}_c = \mathrm{diag}\left[\mathbf{M}_1 \quad \mathbf{M}_2 \quad \mathbf{M}_3 \quad \mathbf{M}_4\right]$, and $\mathbf{K}_c = \mathrm{diag}\left[\mathbf{K}_1 \quad \mathbf{K}_2 \quad \mathbf{K}_3 \quad \mathbf{K}_4\right]$.

If $\mathbf{M}_c$ and $\mathbf{K}_c$ are partitioned and sorted according to the dependent and independent variables $\boldsymbol{\theta}^{(d)}$ and $\boldsymbol{\theta}^{(i)}$, the kinetic and potential energies can then be written as

$$T_c = \frac{1}{2}\begin{Bmatrix} \dot{\boldsymbol{\theta}}^{(i)} \\ \dot{\boldsymbol{\theta}}^{(d)} \end{Bmatrix}^{\mathrm{T}} \begin{bmatrix} \mathbf{M}_c^{(ii)} & \mathbf{M}_c^{(id)} \\ \mathbf{M}_c^{(di)} & \mathbf{M}_c^{(dd)} \end{bmatrix} \begin{Bmatrix} \dot{\boldsymbol{\theta}}^{(i)} \\ \dot{\boldsymbol{\theta}}^{(d)} \end{Bmatrix}, \tag{19}$$

$$V_c = \frac{1}{2}\begin{Bmatrix} \boldsymbol{\theta}^{(i)} \\ \boldsymbol{\theta}^{(d)} \end{Bmatrix}^{\mathrm{T}} \begin{bmatrix} \mathbf{K}_c^{(ii)} & \mathbf{K}_c^{(id)} \\ \mathbf{K}_c^{(di)} & \mathbf{K}_c^{(dd)} \end{bmatrix} \begin{Bmatrix} \boldsymbol{\theta}^{(i)} \\ \boldsymbol{\theta}^{(d)} \end{Bmatrix}. \tag{20}$$

2.5. System equations of motion

Across the interface between two adjacent segments, the following continuity and equilibrium conditions must be satisfied

$$\begin{Bmatrix} \theta_n^{(d)} \\ \theta'^{(d)}_n \end{Bmatrix} = \mathbf{C}_n \begin{Bmatrix} \theta_n^{(i)} \\ \theta'^{(i)}_n \end{Bmatrix}, \tag{21}$$

where

$$\mathbf{C}_n = \begin{bmatrix} 1 & 0 \\ 0 & J_{n+1}^4/J_n^4 \end{bmatrix},$$

J_n and J_{n+1} are the polar moments of area of cross sections for segments n and $n+1$, respectively. The constraint equations for the entire crankshaft can be obtained in the following vector form:

$$\mathbf{g} = \boldsymbol{\theta}^{(d)} - \mathbf{C}\cdot\boldsymbol{\theta}^{(i)} = \mathbf{0}, \tag{22}$$

where $\mathbf{C} = \mathrm{diag}[\,\mathbf{C}_1 \quad \mathbf{C}_2 \quad \mathbf{C}_3\,]$ is the global constraint matrix.

The kinetic energy of the dynamical system is

$$T = T_1 + T_c + T_p, \tag{23}$$

where the kinetic energy of the propeller assembly, T_p, is

$$T_p = \frac{1}{2} I_p \dot{\theta}_p^2, \tag{24}$$

where I_p is the mass moment of inertia of the propeller assembly including the propeller, the torque plate, the washer, the extension nut and the portion of the crankshaft covered by the propeller assembly. The value of I_p can be found in Table 2.

The potential energy of the system mainly comes from the crankshaft. There are also intake/exhaust-valve control springs in the engine. Calculations indicate that their potential energy is insignificant and can be omitted in the system dynamics. The potential energy of the system is

$$V = V_c, \tag{25}$$

where V_c is defined in Eq. (20).

The equations of motion can be derived from the augmented Lagrange equations [23,25] as

$$\frac{\mathrm{d}}{\mathrm{d}t}\left(\frac{\partial L}{\partial \dot{\boldsymbol{\theta}}^{\mathrm{T}}}\right) - \frac{\partial L}{\partial \boldsymbol{\theta}^{\mathrm{T}}} - \mathbf{G}^{\mathrm{T}}\boldsymbol{\lambda} - \mathbf{q} = \mathbf{0}, \tag{26}$$

where $L = T - V$ is the Lagrangian, $\boldsymbol{\lambda}$ is the Lagrange multiplier vector; $\boldsymbol{\theta} = \{\boldsymbol{\theta}^{(i)}, \ \boldsymbol{\theta}^{(d)}\}^{\mathrm{T}}$, $\mathbf{G} = \partial \mathbf{g}/\partial \boldsymbol{\theta}^{\mathrm{T}} = \begin{bmatrix} -\mathbf{C} & \mathbf{I} \end{bmatrix}$, $\mathbf{q}$ is the generalized force vector, including the gas torque Q given in Eq. (9) and the aerodynamic load Q_p given in Eq. (10). The equations of motion of the constrained system are

$$\begin{bmatrix} \mathbf{M}_c^{(ii)} & \mathbf{M}_c^{(id)} \\ \mathbf{M}_c^{(di)} & \mathbf{M}_c^{(dd)} \end{bmatrix} \begin{Bmatrix} \ddot{\boldsymbol{\theta}}^{(i)} \\ \ddot{\boldsymbol{\theta}}^{(d)} \end{Bmatrix} + \begin{bmatrix} \mathbf{K}_c^{(ii)} & \mathbf{K}_c^{(id)} \\ \mathbf{K}_c^{(di)} & \mathbf{K}_c^{(dd)} \end{bmatrix} \begin{Bmatrix} \boldsymbol{\theta}^{(i)} \\ \boldsymbol{\theta}^{(d)} \end{Bmatrix} - \begin{Bmatrix} -\mathbf{C}^{\mathrm{T}}\boldsymbol{\lambda} \\ \boldsymbol{\lambda} \end{Bmatrix} + \begin{Bmatrix} \mathbf{h} \\ \mathbf{0} \end{Bmatrix} = \mathbf{0}. \tag{27}$$

Substituting Eq. (22) into Eq. (27) and eliminating $\boldsymbol{\theta}^{(d)}$ and $\boldsymbol{\lambda}$, the equations of motion are reduced to the following equations that only contains $\boldsymbol{\theta}^{(i)}$,

$$\mathbf{M}\ddot{\boldsymbol{\theta}}^{(i)} + \mathbf{K} \cdot \boldsymbol{\theta}^{(i)} + \mathbf{h} = \mathbf{0}, \tag{28}$$

where

$$\begin{aligned} \mathbf{M} &= \mathbf{M}^{(ii)} + \mathbf{M}^{(id)}\mathbf{C} + \mathbf{C}^{\mathrm{T}}\mathbf{M}^{(di)} + \mathbf{C}^{\mathrm{T}} \cdot \mathbf{M}^{(dd)}\mathbf{C}, \\ \mathbf{K} &= \mathbf{K}^{(ii)} + \mathbf{K}^{(id)}\mathbf{C} + \mathbf{C}^{\mathrm{T}}\mathbf{K}^{(di)} + \mathbf{C}^{\mathrm{T}}\mathbf{K}^{(dd)}\mathbf{C}, \\ \mathbf{h} &= \left\{ I\ddot{\theta}_1^{(i)} + \frac{1}{2} I' \dot{\theta}_1^{(i)2} - Q \quad 0 \cdots 0 \quad I_p \ddot{\theta}_p^{(i)} + Q_p \quad 0 \right\}^{\mathrm{T}}. \end{aligned}$$

For convenience, superscript (i) in $\boldsymbol{\theta}^{(i)}$ is dropped in the following sections.

3. Reduction of degrees of freedom

Linear time integration scheme such as the Newmark method is known to be inadequate when large nonlinearities present as those in the equations of motion in above sections. The large number of degrees of freedom prevents the direct use of accurate nonlinear time integration schemes. This conflict can be resolved through the use of component mode synthesis.

The highest frequency of excitation in the driving forces expressed using 40-term Fourier series is 20 harmonics of the mean speed of the crankshaft. Finely tuned engine can reach a maximum mean speed of 8000 rev/min with a 24″ diameter and 6″ pitch propeller, which gives out the highest possible excitation frequency of 2667 Hz. The fundamental and the second natural frequencies of the crankshaft are estimated to be around 800–1000 and 26000–28000 Hz, if the engine is regarded as a constant mass. It is known that the variation of the mass moment of inertia will only change these frequencies slightly; hence the possible internal resonance will only happen at the same magnitude of the fundamental natural frequency of the crankshaft.

Consequently, only lower torsional modes of the crankshaft need to be retained in the system response. This significantly reduces the total number of degrees of freedom. The reduced set of differential equations can then be solved using a nonlinear integration scheme.

The component mode synthesis requires that some degrees of freedom are chosen as interface degrees of freedom, while others as internal degrees of freedom. The motion of internal degrees of freedom can be related to the motion of interface degrees of freedom and internal modes. Since the nonlinear terms in Eq. (28) are related only to θ_1 and θ_p, these variables are chosen as interface degrees of freedom. Denoting the interface degrees of freedom with a subscript f and internal degrees of freedom with a subscript t, Eq. (28) can be rewritten as

$$\begin{bmatrix} \mathbf{M}_{tt} & \mathbf{M}_{tf} \\ \mathbf{M}_{ft} & \mathbf{M}_{ff} \end{bmatrix} \begin{Bmatrix} \ddot{\boldsymbol{\theta}}_t \\ \ddot{\boldsymbol{\theta}}_f \end{Bmatrix} + \begin{bmatrix} \mathbf{K}_{tt} & \mathbf{K}_{tf} \\ \mathbf{K}_{ft} & \mathbf{K}_{ff} \end{bmatrix} \begin{Bmatrix} \boldsymbol{\theta}_t \\ \boldsymbol{\theta}_f \end{Bmatrix} + \begin{Bmatrix} \mathbf{0} \\ \mathbf{h}_f \end{Bmatrix} = \mathbf{0}, \tag{29}$$

where

$$\boldsymbol{\theta}_t = \begin{Bmatrix} \theta_1' & \theta_2 & \theta_2' & \cdots & \theta_{p-1} & \theta_{p-1}' & \theta_p' \end{Bmatrix}^{\mathrm{T}}, \quad \boldsymbol{\theta}_f = \begin{Bmatrix} \theta_1 & \theta_p \end{Bmatrix}^{\mathrm{T}}, \quad \mathbf{h}_f = \begin{Bmatrix} I\ddot{\theta}_1 + \frac{1}{2}I'\dot{\theta}_1^2 - Q \\ I_p\ddot{\theta}_p + Q_p \end{Bmatrix}.$$

If the interface is fixed by letting $\boldsymbol{\theta}_f = \mathbf{0}$, the first set of equations in Eq. (29) is reduced to

$$\mathbf{M}_{tt}\ddot{\boldsymbol{\theta}}_t + \mathbf{K}_{tt}\boldsymbol{\theta}_t = \mathbf{0}. \tag{30}$$

An eigenanalysis for Eq. (30) can be easily conducted. Let $\boldsymbol{\Lambda}_t$ be the diagonal matrix with each diagonal element representing a natural frequency of the internal system, and $\boldsymbol{\Phi}_t$ be the modal matrix normalized with respect to the mass matrix $\mathbf{M}_{tt}$. Each column of the modal matrix represents a normalized modal vector corresponding to the diagonal element in matrix $\boldsymbol{\Lambda}_t$.

Under the fixed interface condition, a solution for the internal degrees of freedom can be written as

$$\boldsymbol{\theta}_t^{(1)} = \boldsymbol{\Phi}_t\mathbf{x}, \tag{31}$$

where $\mathbf{x}$ is the modal coordinate vector. Now release the interface, the internal structure will have additional response due to the motion of the interface. That is

$$\boldsymbol{\theta}_t^{(2)} = -\mathbf{K}_{tt}^{-1}\mathbf{K}_{tf}\boldsymbol{\theta}_f = \boldsymbol{\Phi}_f\boldsymbol{\theta}_f. \tag{32}$$

The total response consisting of two responses is written as

$$\boldsymbol{\theta}_t = \boldsymbol{\theta}_t^{(1)} + \boldsymbol{\theta}_t^{(2)} = \boldsymbol{\Phi}_t\mathbf{x} + \boldsymbol{\Phi}_f\boldsymbol{\theta}_f. \tag{33}$$

Then the original variable vector can be expressed as

$$\begin{Bmatrix} \boldsymbol{\theta}_t \\ \boldsymbol{\theta}_f \end{Bmatrix} = \mathbf{T}_s \begin{Bmatrix} \mathbf{x} \\ \boldsymbol{\theta}_f \end{Bmatrix}. \tag{34}$$

where

$$\mathbf{T}_s = \begin{bmatrix} \boldsymbol{\Phi}_t & \boldsymbol{\Phi}_f \\ \mathbf{0} & \mathbf{I} \end{bmatrix}.$$

Now the problem is transformed to a space mixed with modal coordinates $\mathbf{x}$ and interface coordinates $\boldsymbol{\theta}_f$. Since the high-frequency modes are discarded, matrix $\boldsymbol{\Phi}_t$ contains only a few columns of modal vectors. Substituting Eq. (34) into Eq. (30) and pre-multiplying the so-obtained equations by $(\mathbf{T}_s)^{\mathrm{T}}$, the equations of motion can be written as

$$\begin{bmatrix} \mathbf{I} & \overline{\mathbf{M}}_{tf} \\ \overline{\mathbf{M}}_{ft} & \overline{\mathbf{M}}_{ff} \end{bmatrix} \begin{Bmatrix} \ddot{\mathbf{x}}_t \\ \ddot{\boldsymbol{\theta}}_f \end{Bmatrix} + \begin{bmatrix} \boldsymbol{\Lambda}_t & \mathbf{0} \\ \mathbf{0} & \overline{\mathbf{K}}_{ff} \end{bmatrix} \begin{Bmatrix} \mathbf{x}_t \\ \boldsymbol{\theta}_f \end{Bmatrix} + \begin{Bmatrix} \mathbf{0} \\ \mathbf{h}_f \end{Bmatrix} = \mathbf{0}, \tag{35}$$

where $\mathbf{I}$ is an identity matrix. The above reduced equations of motion represent an autonomous differential system. It can be solved efficiently using accurate nonlinear time integration method.

4. Numerical results

4.1. Influence of crankshaft flexibility and varying inertia of the engine block

To study the influence of the crankshaft flexibility, a rigid body model is implemented by ignoring the flexibility of the crankshaft. The single equation of motion, which governs the response of the dynamical system, is written as

$$I\ddot{\theta}_1 + \tfrac{1}{2}I'\dot{\theta}_1^2 = Q - Q_p. \tag{36}$$

The model is numerically solved using the fifth-order Runge–Kutta method with a 6″ pitch setting and 50% throttle opening. The velocity response and its frequency spectrum are shown in Figs. 9 and 10. The response of the system at the propeller under the same settings is also obtained from the flexible model and shown in Figs. 9 and 10 for comparison. The mean speed is deducted from the angular velocity to obtain the velocity fluctuation. The oscillatory velocity is deterministic and hence can be represented by the root-mean square (rms) spectrum. It can be seen that the flexibility of the crankshaft increases the velocity oscillation by introducing a high-frequency component. The frequency spectrum shows that in both models there are responses in all integer and half harmonics. The $1\frac{1}{2}$-order harmonic is the predominant frequency; while in the flexible model, a spike across the $13\frac{1}{2}$- and 14-order harmonics is present. This response is not concentrated at a single frequency but distributes in a narrow band. The varying inertia of the engine block causes the natural frequency of the crankshaft to vary with its angular position. The variation of the fundamental natural

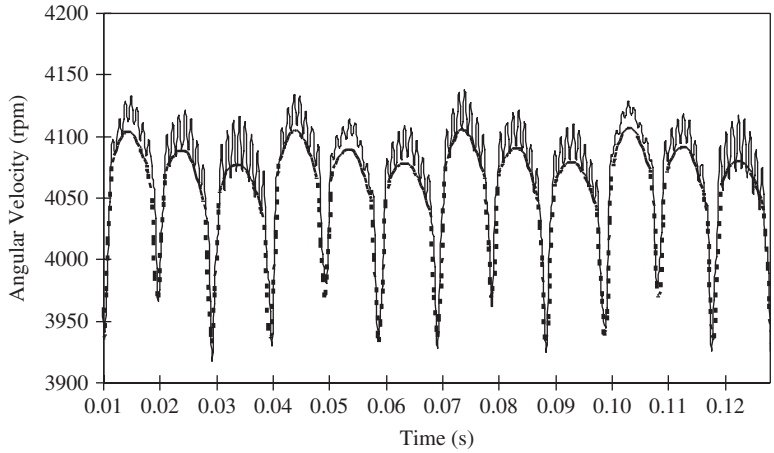

Fig. 9. Angular velocities at the propeller obtained using the rigid body model (----) and flexible model (——).

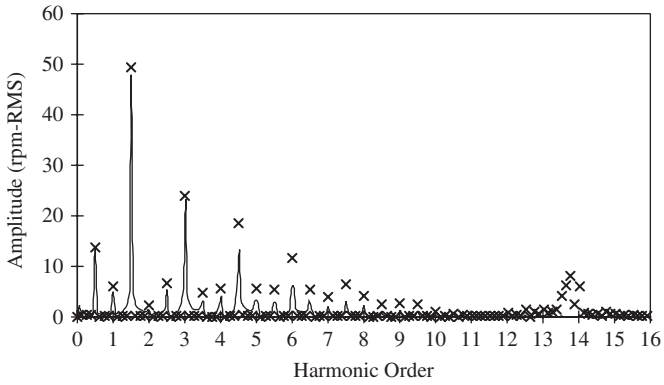

Fig. 10. Comparison of the frequency spectrum of the angular velocity fluctuation at the propeller: rigid body model —; flexible model ×.

frequency of the crankshaft with the crankshaft angular position is shown in Fig. 11. The fundamental natural frequency varies from 896 to 956 Hz in one revolution, which explains the presence of the $13\frac{1}{2}$- and 14-order harmonics.

Another influence of the crankshaft flexibility is the variation of periodicity. If the displacement related to the mean speed is deducted from the total displacement, the rigid body model response is periodic as presented in the phase plot in Fig. 12. However, when crankshaft flexibility is considered, the system motion is no longer periodic, but a bounded motion as demonstrated by the Poincare map in Fig. 13(a). To view this situation more clearly, the Poincare map is extruded along the axis of the crankshaft angle from 0 to 4π (a thermodynamic cycle) and shown in Fig. 13(b). The periodic motion is transferred to a quasi-periodic motion.

The velocity spectrum shows that the flexibility-induced oscillation is small for the higher order harmonics. However, small amplitude high-frequency velocity oscillation leads to a large amplitude oscillation in acceleration and hence a large shear. Comparisons of shear stresses at the torque plate, predicted using the rigid and rigid-flexible models, shown in Fig. 14, indicate that the crankshaft flexibility has a significant effect on the shear stress.

To see the influence of the varying inertia of the engine block, a solution is obtained by ignoring the inertia variation and compared to the previous result that involves the varying inertia, as shown in Fig. 15. It can been seen that the varying inertia has little influence on the velocity response for this particular

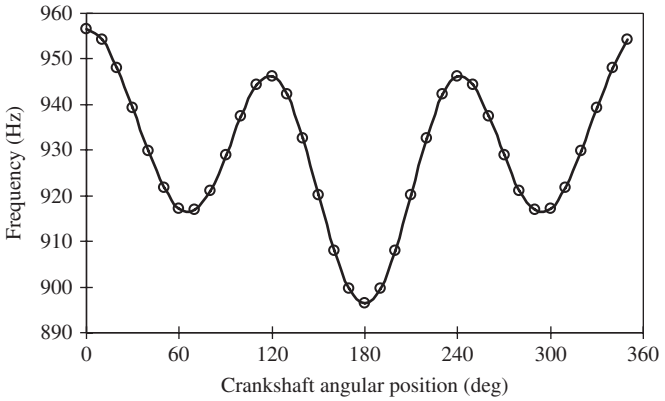

Fig. 11. Crankshaft fundamental natural frequency in one revolution.

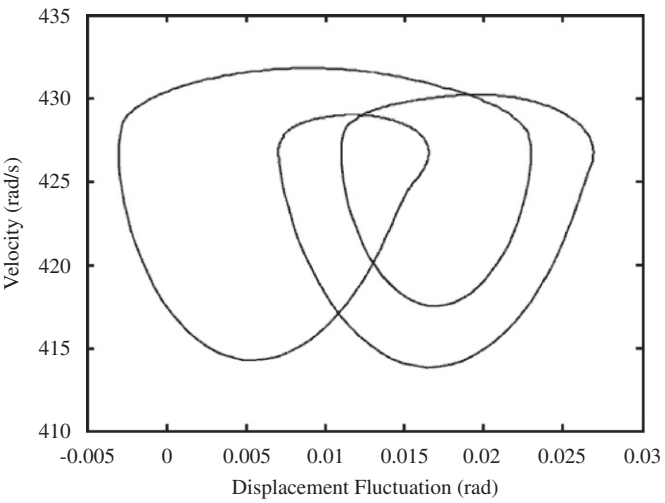

Fig. 12. Phase diagram of the system response: rigid body model.

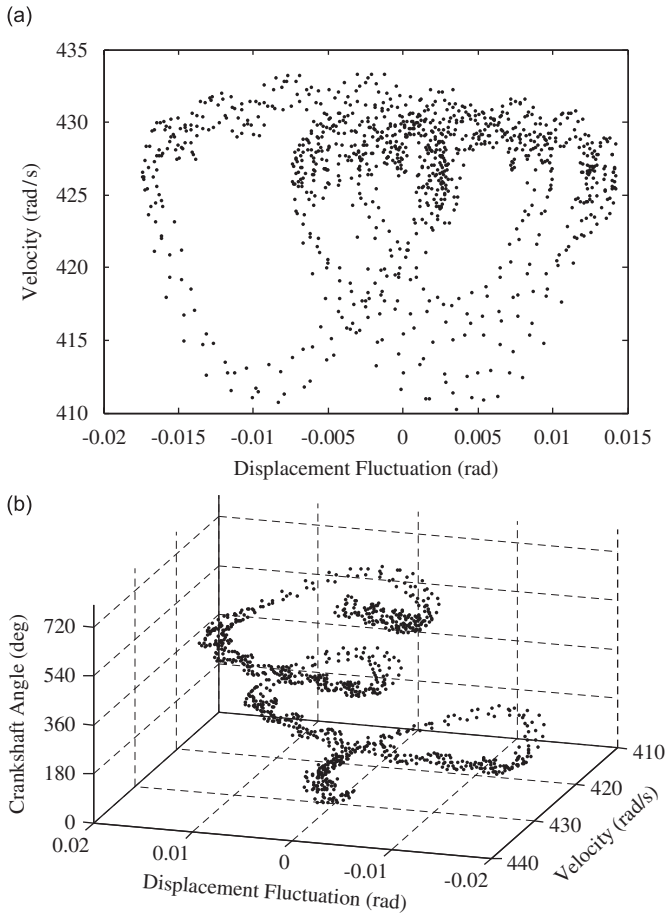

Fig. 13. Poincare map of the flexible model response: (a) Poincare map and (b) Poincare map with crankshaft angle axis.

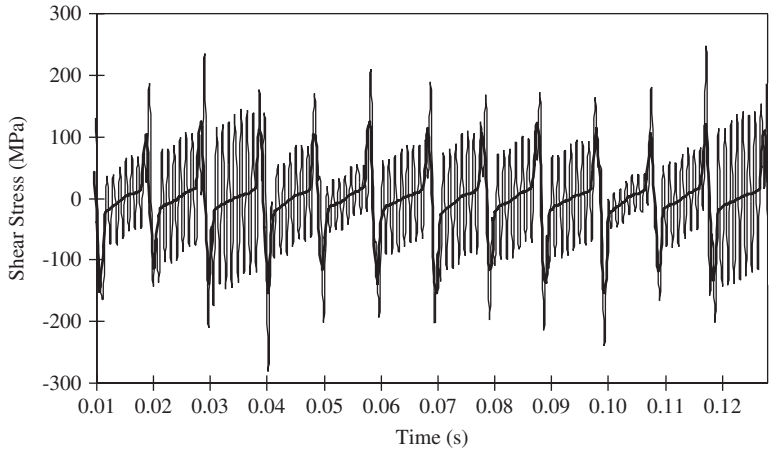

Fig. 14. Maximum shear stress at the interface between the torque plate and the crankshaft: rigid body model ——; flexible model - - - -.

engine–propeller system, since the variation of the effective mass moment of inertia of the engine is only 5% of its mean value and the nonlinear term related to the derivative of the varying inertia in the equations of motion, $I'\dot{\theta}_1^2$, is also small (at the 10^{-5} level).

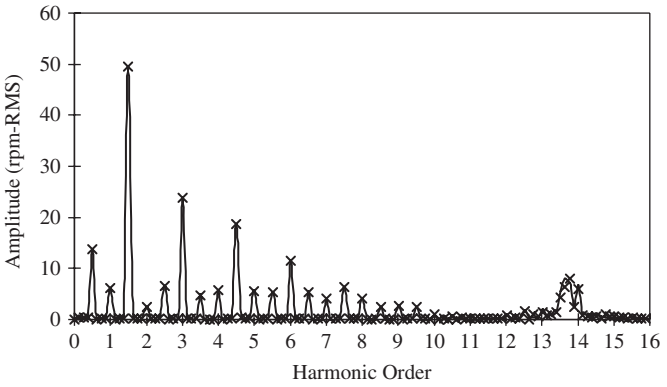

Fig. 15. The influence of the varying engine inertia on the velocity spectrum: without varying inertia —; with varying inertia ×.

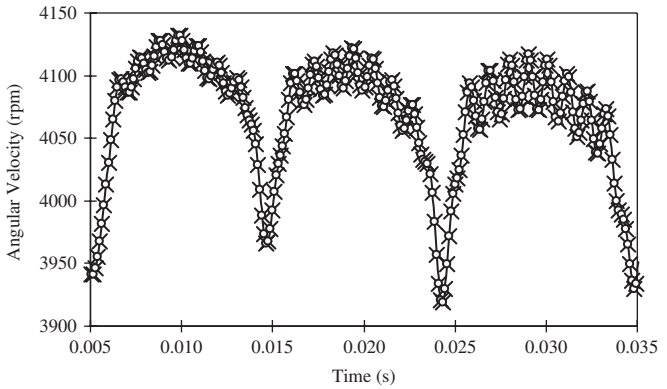

Fig. 16. Comparison of the angular velocity between the full dof model and the reduce dof model in one cycle: without substructuring ——; with 1 internal mode retained ×; with 2 internal mode retained ○.

Table 3
Computing time of the reduced model and the full model for a 0.1 s solution

	Reduced dof model			Full dof model	
	1 mode retained	2 modes retained	3 modes retained	4 finite elements	8 finite elements
Allowed time increment (ms)	0.33	0.17	0.12	0.040	0.041
Computing time (s)	49	108	147	18200	66400

4.2. Efficiency and accuracy of the substructuring method

To demonstrate the accuracy of the substructuring method, velocity responses at the propeller are obtained using the model with full degrees of freedom as specified in Eq. (28), the reduced model with one internal mode, and two internal modes. These three sets of results are compared in Fig. 16. It can be seen that the reduced model even with one internal mode yields satisfactory result. Table 3 shows the computational costs for the full model and the reduced model with different number of internal models retained. The computing times are recorded for 0.1 s simulation duration on a 1.66 GHz personal computer. In comparison with the full model, the substructuring method not only greatly reduces the computing time, but also improves the numerical stability [24]. As a consequence, a larger integration time step can be used to achieve the same level

of accuracy. Another advantage for the substructuring method is that the computing time does not depend on the number of finite elements used, but merely on the number of internal modes retained.

5. Experimental results and discussions

A test rig of the Saito-R450 engine coupled with a variable pitch SOLO propeller (24″ in diameter), shown in Fig. 17, is set up to further study the torsional vibration of the crankshaft. A magnetic encoder (Admotec, KL2202) is installed on the torque plate as shown in Fig. 18, to measure the instant angular velocity of the crankshaft at this location. The magnetic encoder consists of a rotating ring made of ferrous metal and a magnetic sensor. The ring has 64 precisely machined magnetic teeth that provide the code pattern. The nominal pitch angle of the encoder, covering one magnetic tooth and one space, is $\Delta\theta = 2\pi/64$. As the ring rotates with the torque plate, these teeth disturb the magnetic flux emitted by the magnet, and cause the flux field to expand and collapse. These changes in the electromagnetic field are picked up by a sensor. The sensor

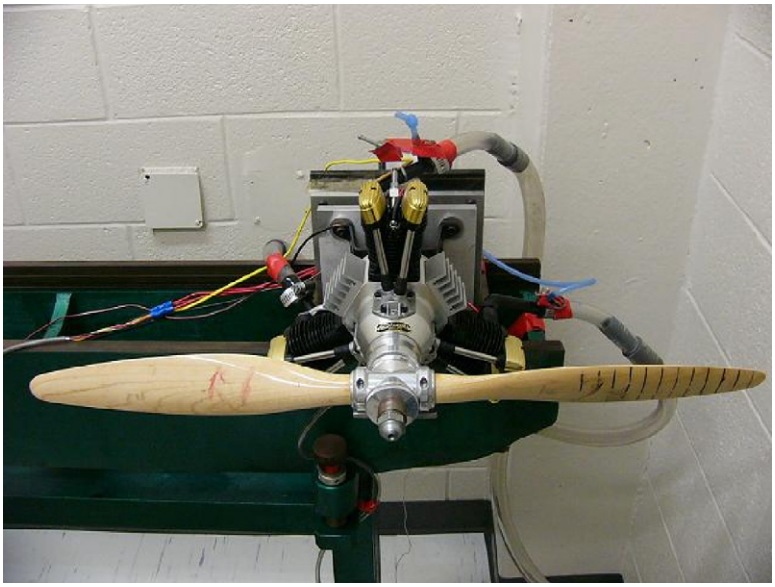

Fig. 17. Experimental setup.

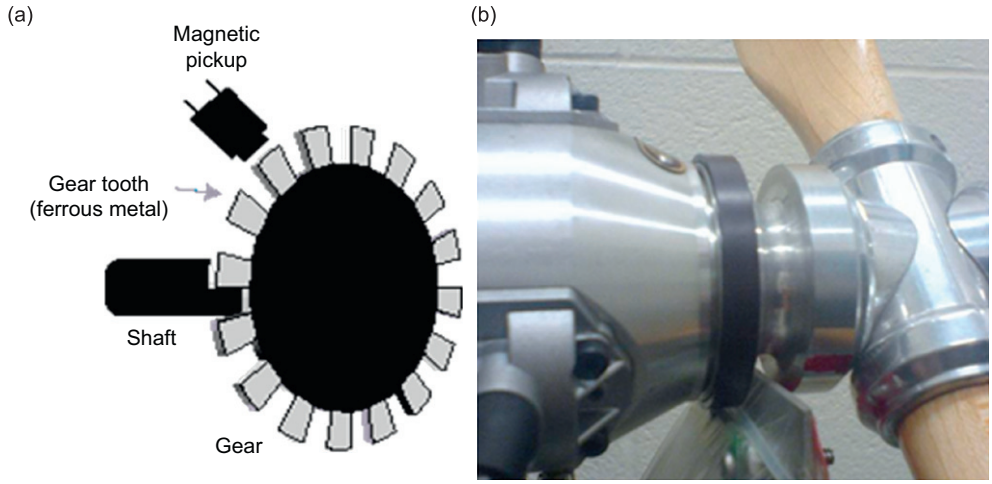

Fig. 18. Magnetic encoder: (a) illustration of the magnetic encoder and (b) mounting position of the magnetic encoder.

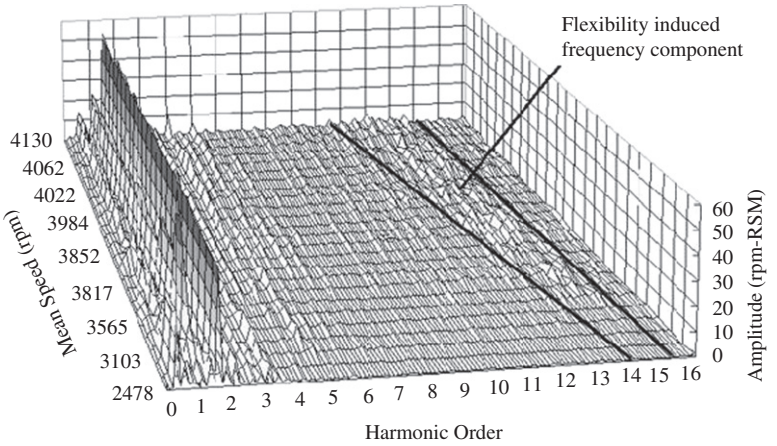

Fig. 19. Frequency spectra of the angular velocity fluctuation at different mean speeds.

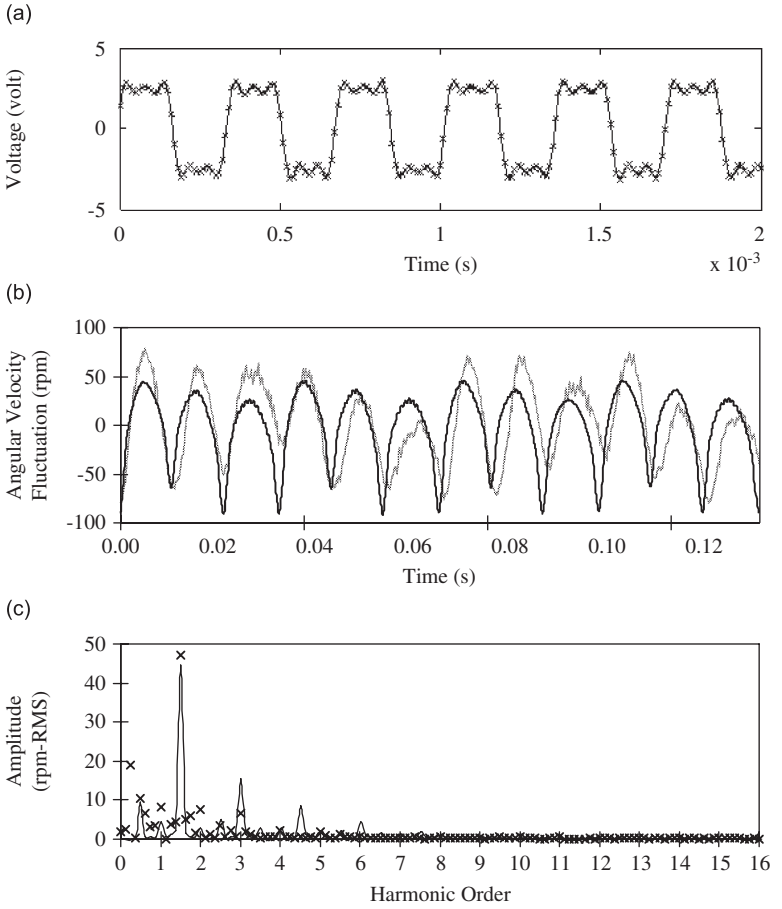

Fig. 20. Comparison of angular velocities between experiment and simulation at a mean speed of 2760 rev/min: (a) the original pulse signal, (b) the angular velocities fluctuation (simulation —, experiments · · ·) and (c) the root-mean-square spectrum of the angular velocity fluctuation (simulation —, experiments ×).

generates a pulse signal instantly in accordance with the teeth and spaces arrive at the sensor location. The full scale output is a 0–5 v electrical signal, but in practice the output is less than full scale due to the high angular speed of the crankshaft. The electrical signal pulse signal is then sampled and stored using a 16 channel data acquisition system having a 16-bit analog-digital converter and a maximum sampling rate of 100 kHz. The output pulse signal is shifted to have a zero mean voltage for the convenience of data processing.

The original signal is a series of pulses with varying widths in time, as shown in Figs. 20(a), 21(a), 22(a) and 23(a). For a brand new engine working in break-in stage, the crankshaft mean speed can be obtained in a range from 2500 to 4500 rev/min. The instant velocity fluctuations are only a few percentages of the mean speed. The pulse width variation is very small and in the same order of sampling interval. To overcome this difficulty, a data processing scheme is developed by utilizing the slopes of the leading edges. The leading edge is curve-fitted using a linear polynomial. The intersection between the polynomial and the 0 v line is found; and the time is recorded. The instant angular velocity at the midpoint in time between the arrival times of two consecutive leading edges is taken to be the ratio of the pitch angle $\Delta\theta$ to the elapsed time. Since the main portion of the leading edge is always a straight line, and the sampling rate of 100 kHz is high enough to ensure that there are more than three data points on the main portion; and the linear polynomial is enough for obtaining the arrival time.

Using the experimental setup and the data processing scheme, angular velocities and their spectra for different mean speeds are obtained. Fig. 19 shows the spectra of the angular velocity fluctuation of the crankshaft at the torque plate at different mean speeds from 2478 to 4130 rev/min. The $1\frac{1}{2}$-order harmonic is

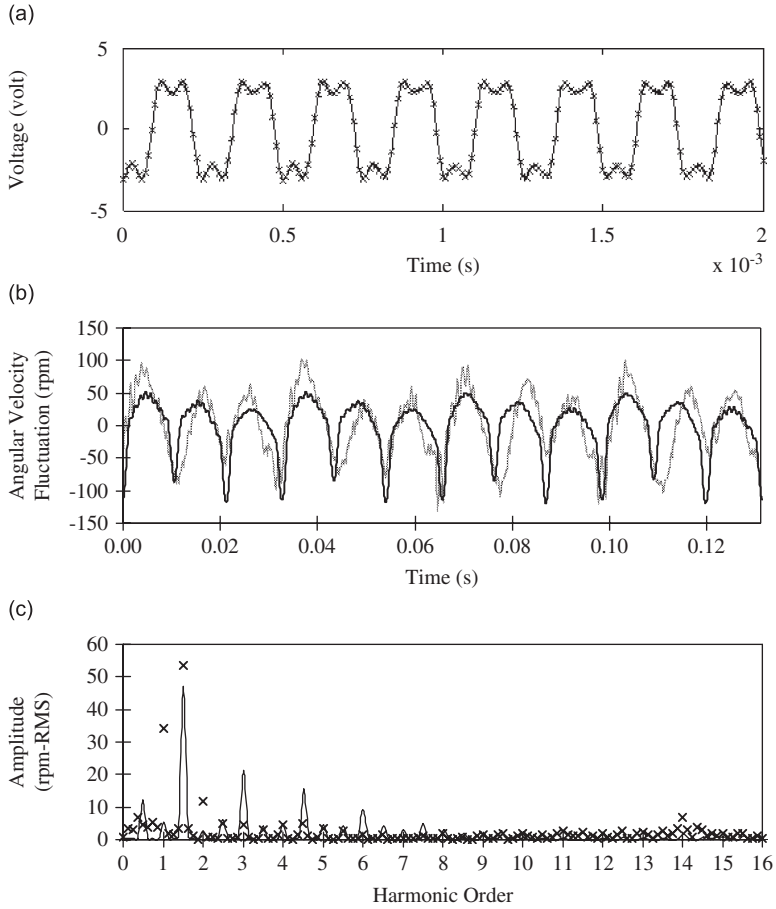

Fig. 21. Comparison of angular velocities between experiment and simulation at a mean speed of 3640 rev/min: (a) the original pulse signal, (b) the angular velocity fluctuation (simulation —, experiments · · ·) and (c) the root-mean-square spectrum of the angular velocity fluctuation (simulation —, experiments ×).

the dominant frequency for all cases except for the mean speed of 3293 rev/min, in which case a larger spike appears at the 1-order harmonic. Besides the $1\frac{1}{2}$-order harmonic, spikes at the 1-, 2-, and 3-order harmonics are also visible. For harmonic orders higher than 5, their amplitudes are very small until the harmonic frequency falls in the range of torsional resonance. The resonance harmonic order decreases with the increase of the crankshaft mean speed, since the torsional natural frequency is not affected by the mean speed. The resonant spikes are distributed in a narrow band rather than concentrated on a single frequency.

The experimental data are compared to the simulation results, as shown in Figs. 20–23 for four test cases. It can be seen that there are good agreements between the simulation and experimental results for the $1\frac{1}{2}$-order harmonic for all cases. At very low mean speed (Fig. 20), the resonant frequency component does not appear within the 16-order harmonic. This is because the 16-order harmonic is lower than the fundamental natural frequency of the system. Simulation results show that a resonant peak appears around 20-order harmonic with a small magnitude; however, this cannot be confirmed experimentally due to the limited number of teeth of the magnetic encoder. When the throttle opens wider, the mean speed increases. The flexibility-induced frequency appears within the 16-order harmonic, as can bee seen in Fig. 21. As a consequence, the high-frequency oscillations in velocity increase apparently. When the mean speed keeps increasing, the flexibility-induced frequency components gradually move towards lower order harmonics as shown in Figs. 22 and 23. The amplitude of high-frequency oscillations also increases. The experimental results show that the theoretical models are able to predict the three major spikes induced by the firing in each cylinder in a thermodynamic cycle, and the resonant oscillations in higher order harmonics induced by the crankshaft flexibility. It also

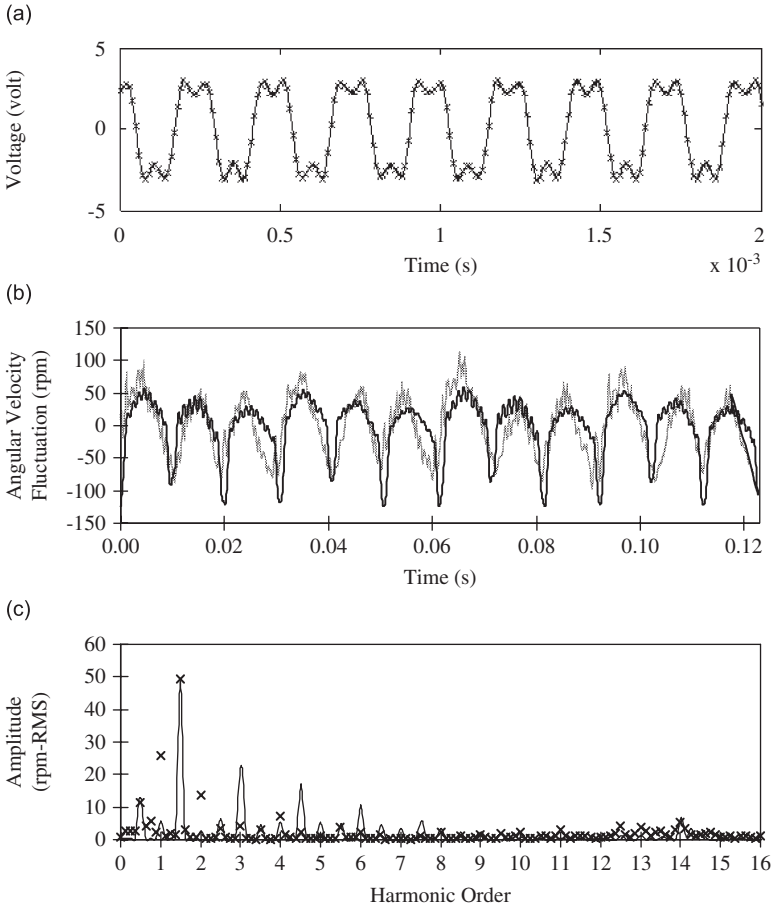

Fig. 22. Comparison of angular velocities between experiment and simulation at a mean speed of 3890 rev/min: (a) the original pulse signal, (b) the angular velocity fluctuation (simulation —, experiments · · ·), and (c) the root-mean-square spectrum of the angular velocity fluctuation (simulation ——, experiments ×).

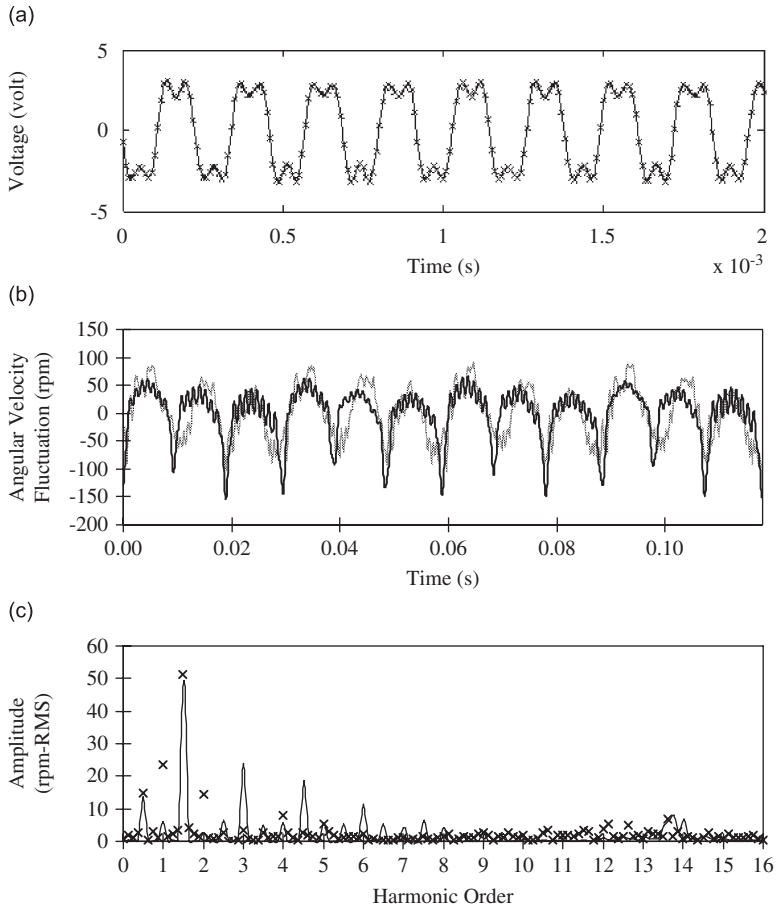

Fig. 23. Comparison of angular velocities between experiment and simulation at a mean speed of 4060 rev/min: (a) the original pulse signal, (b) the angular velocity fluctuation (simulation —, experiments · · ·), and (c) the root-mean-square spectrum of the angular velocity fluctuation (simulation ——, experiments ×).

reveals more information of the system behavior that the theoretical models do not provide, such as the high level of amplitudes at 1- and 2-order harmonics in the velocity response in Figs. 21c, 22c and 23c, and the discrepancy on the 3–6-order harmonics between the theoretical models and the real system. The theoretical models also provide information for understanding the measurement and evaluating the working status of the engine. A fast and accurate strategy for engine monitoring and diagnosis may be implemented by combining the above simulation and experimental procedures.

6. Conclusions

This paper presents theoretical and experimental procedures for investigating the torsional vibration of the crankshaft in an engine–propeller dynamical system. The nonlinearities induced by the varying mass moment of inertia, the propeller aerodynamics and the cylinder gas torque are implemented in a rigid body model. Crankshaft flexibility is further included using finite element method in a flexible body model. Comparisons of the numerical solutions of the two models show the influence of flexibility on the system behavior. The crankshaft flexibility is found to introduce higher order harmonic oscillations in velocities and accelerations due to the resonance between the high-frequency excitation in the gas torque and the fundamental natural frequency of the crankshaft. The high-frequency resonance greatly increases the amplitude of the oscillatory acceleration and shear stress. The varying inertia is found to have limited influence on the amplitude of velocity response, but it causes the natural frequencies of the crankshaft to vary with angular position in 2π.

As a consequence, the high-frequency resonance spreads over a narrow band in the frequency domain, rather than concentrating on a single frequency. The nonlinearities and the crankshaft flexibility introduce uncertainties in the periodicity of the steady state velocity response, turning the periodic motion to quasi-periodic.

The component mode synthesis is employed to reduce the number of degrees of freedom in the flexible body model so that the model can be practically solved using accurate nonlinear time integration methods. Simulation tests show that the reduction scheme is highly efficient and accurate, being able to reduce the computational cost in a few magnitudes, enhance the integration stability, and maintain all the nonlinear properties. The use of component mode synthesis is proved to be beneficial in the numerical analysis of nonlinear dynamical systems.

The experiments performed on a three-cylinder four-stroke engine coupled with a 24″ propeller confirm the findings from the numerical studies of the rigid and flexible body models. Firstly, the dominant harmonic component in the angular velocities in all cases is the $1\frac{1}{2}$-order harmonic, which is consistent with the general understanding for this type of engine. The rigid body type motion of the crankshaft caused by the uneven cylinder firings is captured by the theoretical models. Secondly, the crankshaft flexibility-induced resonance presents itself in the harmonic range that is discernable to the sensing equipment, when the mean speed increases from low to high level. The frequency range of the higher order harmonic oscillations are captured precisely by the flexible body model. The experimental procedure combined with the numerical analysis can be utilized in engine health monitoring and fault diagnosis.

References

[1] C. Xykis, S. Seidlitz, Torsional analysis of a single cylinder gasoline engine, Society of Automotive Engineers Technical Paper Series, International Off-Highway and Powerplant Congress and Exposition, Milwaukee, United States, No. 901637, September 10–13, 1990.

[2] K. Shimoyamada, S. Iwamoto, T. Kodama, Y. Honda, K. Wakabayashi, A numerical simulation method for vibration waveforms of high-speed diesel engine crankshaft system, *Society of Automotive Engineers Transactions* 100 (3) (1991) 933–953.

[3] A.A. Smaili, M.P. Khetawat, Dynamic modeling of automotive engine crankshafts, *Mechanism and Machine Theory* 29 (7) (1994) 995–1006.

[4] Y. Kang, G.J. Sheen, M.H. Tseng, S.H. Tu, H.W. Chiang, Modal analyses and experiments for engine crankshafts, *Journal of Sound and Vibration* 214 (3) (1998) 413–430.

[5] M.S. Pasricha, W.D. Carnegie, Formulation of the equations of dynamic motion including the effects of variable inertia on the torsional vibrations in reciprocating engines—part 1 and 2, *Journal of Sound and Vibration* 66 (2) (1979) 181–186.

[6] E. Brusa, C. Delprete, G. Genta, Torsional vibration of crankshafts: effects of non-constant moments of inertia, *Journal of Sound and Vibration* 205 (2) (1997) 135–150.

[7] P. Metallidis, S. Natsiavas, Linear and nonlinear dynamics of reciprocating engines, *International Journal of Non-Linear Mechanics* 38 (5) (2003) 723–738.

[8] S. Gupta, P. Kelly, H. Rahnejat, Elasto-multi-body dynamics of multi-cylinder internal combustion engine, *Proceedings of ASME International Mechanical Engineering Congress and Exposition*, Vol. 2, New York, United States, November 11–16, 2001, pp. 275–283.

[9] Z.D. Ma, N.C. Perkins, An efficient multibody dynamics model for internal combustion engine systems, *Multibody System Dynamics* 10 (2003) 363–391.

[10] D.M.W. Hoffman, D.R. Dowling, Fully coupled rigid internal combustion engine dynamics and vibration—part 1 and part 2, *Journal of Engineering for Gas Turbine and Power* 123 (2001) 677–692.

[11] A. Carcaterra, R. D'Aquino, Torsional vibration in ship's propulsion device accounting for parametric excitation and propeller-engine coupling, *Proceedings of ISMA23*, Vol. 3, Leuven, Belgium, September 16–18, 1998, pp. 1439–1446.

[12] A.A. Shabana, Flexible multibody dynamics: review of past and recent developments, *Multibody System Dynamics* 1 (2) (1997) 189–222.

[13] R.R. Craig, Coupling of substructures for dynamic analyses: an overview, *Collection of Technical Papers—AIAA/ASME/ASCE/AHS/ASC Structures, Structural Dynamics and Materials Conference*, Vol. 5, Atlanta, USA, April 3–6, 2000, pp. 3–14.

[14] W.C. Hurty, Dynamic analysis of structural systems using component modes, *AIAA Journal* 3 (4) (1965) 678–685.

[15] R.R. Craig, M.C.C. Bampton, Coupling of substructures for dynamic analysis, *AIAA Journal* 6 (7) (1968) 1313–1319.

[16] Z.P. Mourelatos, Efficient crankshaft dynamic analysis using substructuring with Ritz vectors, *Journal of Sound and Vibration* 238 (3) (2000) 495–527.

[17] A.G. Erdman, G.N. Sandor, S. Kota, 4th ed, *Mechanism Design—Analysis and Synthesis*, Vol. 1, Prentice-Hall, Upper Saddle River, NJ, 2001.

[18] J.S. Walker, *Fast Fourier Transforms*, CRC Press, Boca Raton, 1991.

[19] S.A. Warwick, S.D. Yu, Rigid body dynamics of a three-cylinder, four-stroke internal combustion engine coupled with an aircraft propeller, *Proceedings of the Canadian Society for Mechanical Engineering Forum*, Kananaskis, Canada, May 21–24, 2006.
[20] H. Ma, K. Kar, R. Stone, R. Raine, H. Thorwarth, Analysis of combustion in a small homogeneous charge compression assisted ignition engine, *International Journal of Engine Research* 7 (3) (2006) 237–253.
[21] Y.H. Zweiri, J.F. Whidborne, L.D. Seneviratne, Detailed analytical model of a single-cylinder diesel engine in the crank angle domain, *Proceedings of the Institution of Mechanical Engineers, Part D: Journal of Automobile Engineering* 215 (11) (2001) 1197–1216.
[22] S.A. Warwick, Rigid Body Dynamics and Simulation of a Three-cylinder, Four-stroke Internal Combustion Engine Coupled With an Aircraft Propeller, M.A.Sc. Thesis, Ryerson University, 2005.
[23] B. Simeon, On Lagrange multipliers in flexible multibody dynamics, *Computer Methods in Applied Mechanics and Engineering* 195 (2006) 6993–7005.
[24] K. Dekker, J.G. Verwer, *Stability of Runge–Kutta Method for Stiff Nonlinear Differential Equations*, North-Holland Publishing, Amsterdam, 1984.
[25] A.A. Shabana, *Dynamics of Multibody Systems*, Wiley, New York, 1989.